Materials Reports: Solidwaste and Ecomaterials

Journal Homepage: www.sciopen.com/journal/3078-4093

Original Research Report

Influence of CO_3^{2-} and SO_4^{2-} on the chloride binding capacity of AAMs with municipal solid waste incineration fly ash

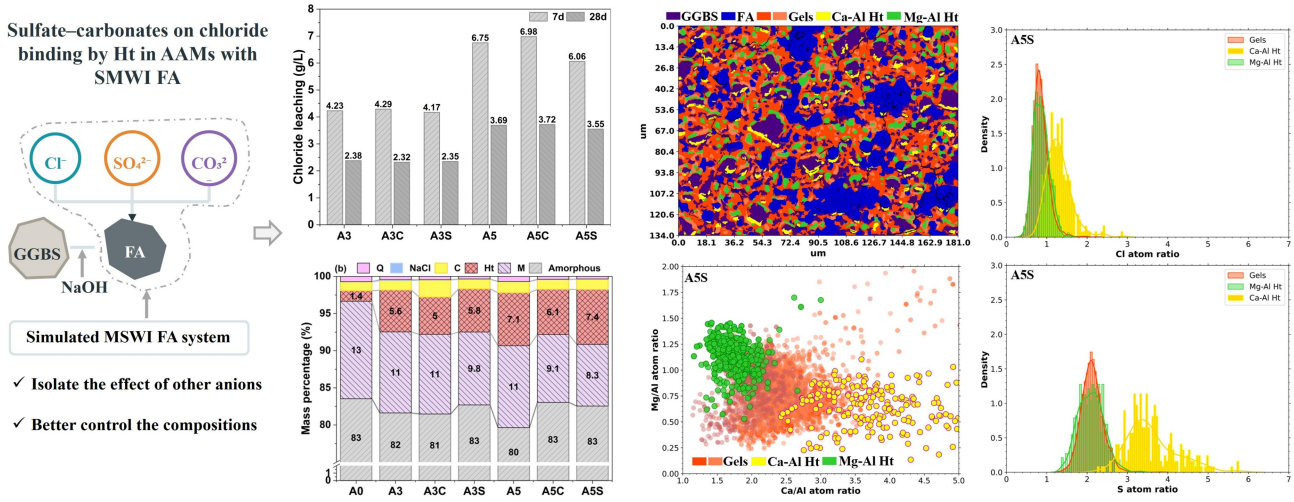
Yu Chen[1], Dezhi Zhao[1, 2], Teng Ma[1], Zhengxin Chen[1, 2], Caihong Xue[1, 2, *], Qingxin Zhao[1, 2]

[1] State Key Laboratory of Metastable Materials Science and Technology, Yanshan University, Qinhuangdao 066000, China

[2] Hebei Province Engineering Research Center for Harmless Synergistic Treatment and Recycling of Municipal Solid Waste, Yanshan University, Qinhuangdao 066004, China

*Corresponding Author: C. Xue (caihongxue@ysu.edu.cn)

Graphical abstract



Abstract: Alkali-activated materials (AAMs) are widely used for the treatment of chloride-rich municipal solid waste incineration fly ash (MSWI FA). However, there is a lack of study on the influence of inevitable CO_3^{2-} and SO_4^{2-} from MSWI FA on the chloride binding capacity of AAMs. In this study, AAMs with different levels of internal Cl^-, SO_4^{2-} and CO_3^{2-} were prepared to simulate the systems with MSWI FA to provide insights into the intricate competition of three anions for being bound by in-situ formed hydrotalcites (Ht) in AAMs. The results showed that at 5 wt% internal Cl^-, CO_3^{2-} reduced bound chloride by 0.81~3.4%, whereas SO_4^{2-} increased it by 3.7~10.2%, and the influence of both anions decreased with prolonging curing time from 7d to 28d. Ht formation in AAMs with 3 wt% Cl^- increased from 5.6 wt% to 6.3 wt% and to 7.1 wt% with the presence of CO_3^{2-} and SO_4^{2-}, respectively, while an increase in Cl^- from 3 wt% to 5 wt% slightly varied the Ht content. Cold-

Citation: Y. Chen, D. Zhao , T. Ma, Z. Chen, C. Xue, Q. Zhao. Influence of CO_3^{2-} and SO_4^{2-} on the chloride binding capacity of AAMs with municipal solid waste incineration fly ash. *Materials Reports: Solidwaste and Ecomaterials*, 2026, 2: 9520042. https://doi.org/10.26599/MRSE.2026.9520042.

Received 13 October 2026; Received in revised form 27 October 2026; Accepted 12 November 2026

water extraction for chloride binding capacity quantification varied the phase assemblage due to dissolution, and the optimal extraction time was 2h for powder samples. Spatial distribution of Ht was obtained by quantitative SEM-EDS hypermaps analysis, which revealed that Ca-Al Ht and Mg-Al Ht coexisted around GGBS, but Cl^- and SO_4^{2-} showed preference for intercalation into the Ca-Al Ht. The SO_4^{2-} from dissolved GGBS competed with Cl^- for intercalating into Ht, and the statistic distribution of S and Cl in the Ht formed in AAMs was probably independent of the relative concentration of two anions in the raw materials. The findings suggest that stabilizing the sulfate by other phases rather than Ht to reduce the competition with chloride is vital to achieve high chloride binding by Ht in AAMs with MSWI FA.

Keywords: Hydrotalcite; Chloride binding; Spatial zonation; Alkali-activated materials

1. Introduction

In alkali-activated materials (AAMs) with GGBS, one of the key secondary reaction products responsible for binding Cl^-, SO_4^{2-}, CO_3^{2-} is the hydrotalcite (Ht), one type of commonly known layered double hydroxides (LDHs) with a Mg-Al double-layered structure [1,2]. The interlayer of Ht, formed by layers of hydroxide ions incorporating divalent Mg^{2+} and trivalent Al^{3+}, carries a net positive charge and can accommodate a variety of anions including OH^-, Cl^-, NO_3^-, CO_3^{2-} and SO_4^{2-} for charge compensation via anion-exchange [3]. It is worth noting that with the development of alkali-activated materials (AAMs) as well as other new sustainable binders, Fe(Ⅱ) doped Ht [4], Ca-Al Ht [5] and Mg-Fe Ht [6] were also identified. Ht contributes to anion binding by both chemical binding within the interlayer and physical adsorption on the laminate surface [7]. The previous study on synthesized Ht confirmed the stability of these anions in Ht with an increasing order of SO_4^{2-}<Cl^-<NO_3^-<OH^-<CO_3^{2-} [8]. That order suggested the preference for anions to be bound by Ht in the pore solution of binders with multiple ions. However, the competition between these anions is far more complicated than that order [9].

It was recently quantified that the presence of OH^- induced the desorption of more than 60% of the chemically bound chloride in synthetic Ht, leading to the fact that 85% of the total chloride uptake in Ht was attributed to physical adsorption in alkali environments [10,11]. Molecular insights into sulfate-induced chloride release from Friedel's salt (one type of Ht in cement systems) reported by Shen et al. [12] demonstrate that SO_4^{2-} weakens both the electrostatic binding of Cl^- to the $[Ca_2Al(OH)_6]^+$ layer and its hydrogen bonding with water in the $[Cl{\cdot}2H_2O]^-$ layer through charge redistribution effect, thereby facilitating Cl^- release and subsequent SO_4^{2-} substitution. In addition, extensive previous experimental studies on cement systems exposed to mixed salts also confirmed the same detrimental effect of SO_4^{2-} on the stabilization of bound chloride, which was attributed to transformation of Friedel's salt to ettringite [13,14]. Different from these cases exposed to external

mixed anions [15,16], Ht formation in AAMs requires the dissolved Al with octahedral coordination from GGBS [17], and this process is accompanied by the release of sulfate from GGBS, which implies that sulfate is likely to intercalate with the $Al(OH)_4^-$ to eliminate the sites for Ht to uptake the chloride from external exposure environment. Moreover, with the incorporation of chloride-rich solid wastes such as soda residue [18] and municipal solid waste incineration fly ash [19,20] in AAMs, chloride, sulfate and carbonates could simultaneously dissolve from these solid wastes at the start of mixing, which could alter the formation and anions binding behavior of Ht.

Extensive previous studies on Ht in AAMs mainly focused on the influence of cations sources such as the content of MgO-rich minerals and Al-rich activators [21-23]. Mg-Al Ht formation is induced when the MgO content in GGBS is higher than 5 wt%, and the Mg/Al atom ratio of Ht typically ranges from 2.1 to 2.6, which is contingent on the composition of the raw materials [24,25]. Liu et al. [26,27] incorporated sodium aluminate in the activator to enhance the chloride adsorption capacity of NaOH-activated GGBS by increasing the Mg-Al Ht content. The corresponding microstructure analysis revealed that the extra $Al(OH)_4^-$ from the activator in a relatively low pH environment at around 12.7 prevents the competition between Mg^{2+} and Si-O tetrahedra for $Al(OH)_4^-$, leading to increased Ht and gel formation at the same time. Furthermore, the mutual inhibition effect between calcium-sodium aluminosilicate hydrate and Ht during precipitation in NaOH-activated GGBS was investigated to eliminate the loss of workability associated with use of $AlNaO_2$ for promoting Ht formation, and a moderate addition of $NaAlO_2$ with 1% Al_2O_3 was suggested [28]. Adel-Gawwad et al. [29] recently formulated Ht-based binders using limestone powder, high reactive MgO and sodium aluminate, which was composed of more than 24 vol% Ht, and the role of MgO in the phase evolution were elucidated.

Although previous studies on Ht have consistently confirmed the competition between Cl^- and SO_4^{2-} for intercalation into Ht exposed to mixed salt, and the promotion effect of MgO as well as $NaAlO_2$ on its formation, the influence of soluble anions in the raw materials of AAMs remained unclear. Thus, in this study, AAMs with different levels of internal Cl^-, SO_4^{2-} and CO_3^{2-} were prepared to investigate the influence of these anions on chloride binding, phase assemblage, spatial zonation and chemistry of hydrotalcite in AAMs. The employed methods included cold-water extraction for chloride binding quantification, quantitative X-ray diffraction (QXRD), thermogravimetric (TG), and quantitative electron dispersive spectroscopy (EDS) hypermaps analysis for characterizing the content and interlayer anions of Ht.

2. Materials and methods

2.1. Materials

Slag (GGBS) and fly ash (FA) with the oxide composition (determined by X-ray fluorescence)

given in Table 1 were used as the precursors for preparing AAMs, and commercial NaOH pellets were used as the activator. Analytical reagent NaCl (≥99.7%), Na_2CO_3 (≥99.3%) and gypsum (≥99.5%) were used to introduce chloride, carbonate, and sulfate ions during mixing, respectively. It was noted that gypsum instead of sodium sulfate was used as the sulfate source considering that the municipal solid waste incineration fly ash contains gypsum.

Table 1. Chemical composition of the raw materials.

Oxides	CaO	Al_2O_3	SiO_2	MgO	SO_3	Na_2O	Fe_2O_3	K_2O	TiO_2	MnO	LOI
GGBS	33.70	17.10	32.60	7.96	3.21	0.56	1.18	0.57	2.54	0.27	2.14
FA	19.91	18.55	45.11	0.96	0.63	1.43	5.56	0.56	1.04	-	2.25

**LOI=loss on ignition*

2.2. Specimen preparation

The proportions of raw materials for different mixes were provided in Table 2. The Na_2O% level from sodium hydroxide was fixed at 4%. The respective chloride content in A3 and A5 groups was 3 wt% and 5 wt% by mass of precursors. Besides, a small proportion of FA was substituted with sodium carbonate or gypsum to induce 2 wt% of CO_3 (denoted by C in the sample ID) or SO_3 (denoted by S in the sample ID) in the precursors.

Table 2. Mix proportions of AAMs, wt%.

ID	GGBS	FA	Na_2CO_3	Gypsum	NaCl	NaOH	w/b
A0	70.0	30.00	-	-	-	5.16	0.4
A3	70.0	25.05	-	-	4.95	5.16	0.4
A3-C	70.0	21.53	3.53		4.95	5.16	0.4
A3-S	70	20.75		4.30	4.95	5.16	0.4
A5	70	21.76			8.24	5.16	0.4
A5-C	70	18.23	3.53		8.24	5.16	0.4
A5-S	70	17.46		4.30	8.24	5.16	0.4

Note: The w/b ratio referred to the water to the solid mass ratio.

The NaOH pellets were dissolved in tap water 24 hours before mixing to obtain the alkali solution. To prepare paste samples, FA, GGBS, NaCl with sodium carbonate or gypsum were dry mixed in a Hobart mixer at low speed for 60s. Thereafter, the alkali solution was added and mixed at high speed for another 4 minutes. The fresh mix was cast in a 50 ml sealed plastic container and cured at room temperature (20℃) until testing.

2.3. Test method

2.3.1. Water-soluble chloride by cold water extraction

According to Xu et al. [30] the free chloride content measured by water extraction method is

controlled by leaching of pore solution chloride and extraction-induced redistribution of bound chloride. They concluded that for Portland cement pastes, an increase in liquid to solid (L/S) ratio and extraction time and a decrease in particle size led to higher free chloride content, which was attributed to the decomposition of chemically bound chlorides induced by OH^- leaching. However, for AAMs, despite the higher alkalinity at an early age, the alkalinity at 28d and beyond is generally lower than that of Portland cement, which means that the influence of OH^- leaching could be less significant. To verify that, the influence of particle size and extraction time were studied to determine the proper parameters of cold-water extraction for AAMs.

Specifically, samples at 7d and 28d were crushed into particles in a range of 1~2mm, and some of these particles were further ground to powder that could pass a 150 μm mesh. Then, the particles or powders were soaked in deionized water with a L/S of 5. The mixtures were shaken for half of the extraction time and then were rested until the filtration with a syringe filter. Finally, the filtration was acidified using nitric (0.2 wt%) and the chloride concentration was measured using an ion chromatograph (IC) from Metrohm.

2.3.2. Quantitative X-ray diffraction

To prepare the samples for microstructure analysis, the hydration of pastes was stopped at 3d, 7d and 28d using isopropanol. The pastes were crushed to 2-3 mm particles and dried by isopropanol solvent exchange for 7 days (with renewal of the isopropanol after 1 h, 1 day and 3 days) followed by isopropanol evaporation under slight vacuum for more than 7 days. Thereafter, the particles were ground into powder that passed the 80 μm sieve. XRD patterns were obtained using a Bruker D8 Advance X-ray Powder Diffractometer, equipped with a LYNXEYEXE-T detector and CuKα radiation, operating at 40 kV and 40 mA. Scans were recorded at the 5°-80° range at a step size of 0.02°. For quantitative phase analysis using Rietveld refinement, 10 wt% ZnO was intermixed with the powder as internal standard. TOPAS v7 software was used for the QPA, following the steps and suggestions detailed in [31]. Quantitative XRD analysis was performed for powders before and after water-soluble chloride extraction with focus on the crystalline phases.

2.3.3. Thermogravimetry analysis

The same hydration-stopped powder without the internal standard for QXRD was used for the thermogravimetric analysis (TGA). Approximately 50 mg of sample was loaded in the crucible and was heated from 30 °C to 1000 °C at 10 °C/min with a protective N_2 atmosphere at a flow rate of 30 mL/min.

2.3.4. Phase assemblage visualization by quantitative analysis of SEM-EDS hypermaps

To visualize the bound chloride distribution, scanning electron microscopy (SEM) coupled with energy dispersive spectroscopy (EDS) was used to obtain SEM-EDS hypermaps. To prepare the samples, crushed particles after hydration stoppage with isopropanol as mentioned above were impregnated under vacuum in a low viscosity epoxy resin. The epoxy-impregnated samples were

polished with 600, 1200 and 3000 abrasive paper for 10 minutes sequentially. Finally, the surface was polished using diamond suspensions (3 and 1 μm) with deodorized petroleum as a lubricant to obtain high-quality mirror-like surfaces. The polished samples were cleaned in an isopropanol ultrasonic bath and dried under a slight vacuum before being coated with a golden layer of about 10 nm. A Hitachi-3400 N SEM was used with an acceleration voltage of 15 kV, a beam current of 1.2 nA, and a working distance of 15 mm. An Oxford UltimMax 170 EDS detector was employed for EDS hypermaps, which were acquired and quantified using the APEX EDAX software at a resolution of 1024 × 768 pixels over regions of 181×134 μm and a dwell time of 256 μs with an averaging over 12 frames for a total acquisition time of about 1 hour as adopted in [32]. For the quantitative analysis of SEM-EDS hypermaps, the Phate-GMM method proposed by the authors in previous studies [33,34] were used. A brief introduction on the implementation of this method was provided in later sections.

3. Results and discussion

3.1. Water-soluble chloride (Cl^-_w)

Fig. 1 (a) shows the variation in Cl^-_w with extraction time when a 28-day power sample passing 150 μm was used. Prolonging the extraction time from 20 minutes to 2h only led to a slightly higher Cl^-_w, but a continuous increase in extraction time from 2h to 24 h resulted in a slight reduction in Cl^-_w, which could be attributed to continuous hydration during the extraction. Nevertheless, the differences in the measured chloride content extracted at three durations were limited to 0.5~5.1% (using the 2h-value as reference), which indicated that in a range of 20 min to 24h, the influence of extraction time was insignificant. Referring to [30,35], the required extraction time to obtain the maximum Cl^-_w increased with the particle size. When particles were larger than 0.63 mm, the extracted free chloride content was only 70% of the maximum content at an extraction time of 30 min. Thus, for the 28-day particles in a range of 1~2mm used in this study, the extraction time investigated was increased to 2d, 7d and 14d, and the results were shown in Fig. 1 (b). A slight increase in Cl^-_w with increasing extraction time from 2d to 7d was observed, but a further increase in extraction time from 7d to 14d resulted slight decrease in Cl^-_w, which was consistent with the trend in Fig. 1 (b). Therefore, the extraction time needed to reach 7d for particle samples. Comparing Fig. 1 (a) and Fig. 1 (b), a lower Cl^-_w was obtained when particle samples were used for cold-water extraction even at sufficient extraction time. However, the difference in the maximum Cl^-_w from powder samples and particles was ~4.3% for A5 (3.89 vs 3.73), ~2.1% (3.89 vs 3.81) for A5C and was ~0.5 for A5S (3.63 vs 3.61), which was insignificant. Also, the lowest Cl^-_w was consistently found in A5S at a chloride content of 5 wt%, which was independent of the extraction time and particle size.

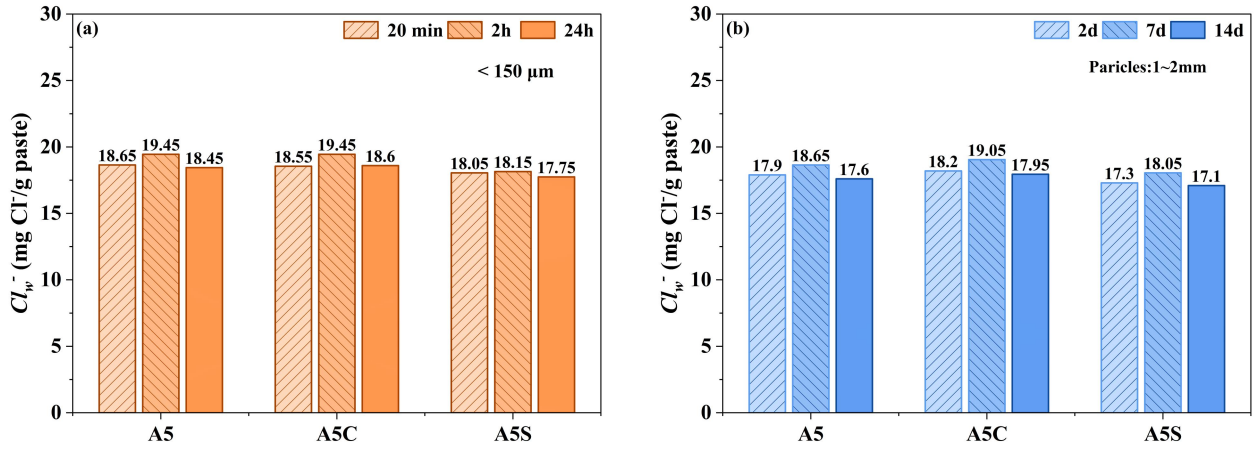


Fig. 1. Effect of cold water-extraction time on the water-soluble chloride in hardened pastes (mg Cl^-/g paste): (a) 28-day powder samples passing 150 μm and (b) 28-day particles samples in a range of 1~2mm.

Using powder samples and an extraction time of 24h, the influence of curing time on chloride binding was studied. Fig. 2 shows the effect of CO_3^{2-}, SO_4^{2-} and curing time on Cl^-_w, where a significant reduction with increasing the curing time from 7d to 28d was observed. The reduction in Cl^-_w from 7d to 28d was around 44% at a chloride content of 3 wt% and was around 45% at a chloride content of 5 wt%, suggesting increasing chloride binding capacity with curing time. The ratio of Cl^-_w at 7d in A3 to A5, A3C to A5C, and A3S to A5S was 0.63, 0.61 and 0.69 respectively, close to the ratio of chloride in the raw materials (0.60), which implied that the chloride binding capacity of AAMs was probably already reached the maximum at a chloride content of 3 wt% in the raw materials. The difference in Cl^-_w of A3, A3C and A3S was in a small range of 11.60 to 11.90, which suggested the influence of CO_3^{2-} and SO_4^{2-} on chloride binding was insignificant at 3 wt% internal chloride. However, the comparison of A5 and A5S indicated that the presence of sulfate reduced the Cl^-_w, but the reduction was limited to 10.2% at 7d and 3.8% at 28d. Contrarily, the higher Cl^-_w in A5C suggested slight increasing effect of CO_3^{2-} on the Cl^-_w.

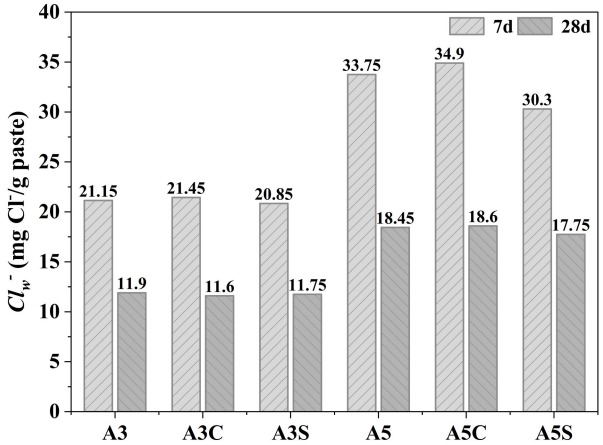


Fig. 2. Effect of CO_3^{2-} and SO_4^{2-} on the water-soluble chloride in hardened pastes (mg Cl^-/g paste).

3.2. Microstructure analysis

3.2.1. QXRD

Fig. 3 shows the XRD patterns of the samples with and without 3 wt% internal chloride before and after cold water extraction. In Fig. 3 (a) hydrotalcite-like phases (Ht) with typical peaks located at about 11.24 (2θ) [29] were detected in all samples. In alkali-activated GGBS, the reaction between dissolved Mg^{2+} and Al^{3+} from GGBS and OH^- from the activator leads to the formation of Ht [24]. Without the presence of other anions in A0, OH^- occupied the interlayer of Ht to achieve electrostatic neutrality. Among the four samples, the highest peak was observed in A3C, which was followed by the peak in A3S and A3. The higher Ht peaks in A3, A3C and A3S as compared to that of A0 suggested that the presence of Cl^-, CO_3^{2-} and SO_4^{2-} increased the formation Ht. In addition, mullite was from the used fly ash, and ZnO was the internal standard added for QXRD. In Fig.3 (a), NaCl was detected in all samples with internal chloride, indicating that the chloride binding capacity of the AAMs was already reached the maximum when the raw materials contained 3 wt% free chloride. Fig.3 (b) shows the XRD patterns of samples subjected to cold-water extraction for water-soluble chloride. The absence of NaCl peaks and other chloride salt peaks confirmed that the cold-water extraction method used in this study extracted all water-soluble chloride.

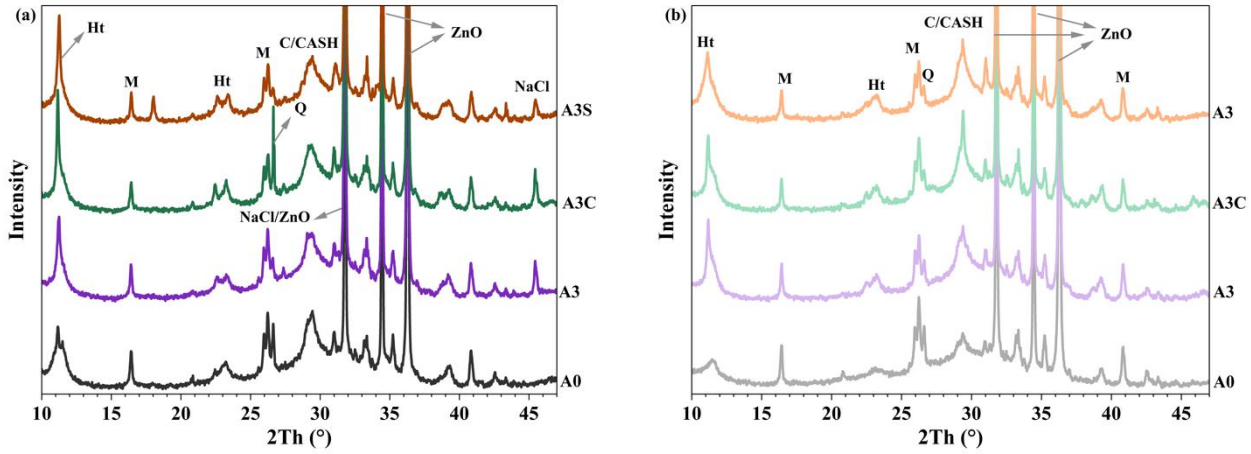


Fig. 3. XRD patterns of samples with 3 wt% internal chloride at 28d (a) before and (b) after cold-water extraction for water-soluble chloride (Ht=hydrotalcite, COD=9009353; M=mullite, COD=9005502; C=Calcite, COD=1010962；CASH=calcium aluminate silicate hydrates; NaCl, COD=1000041; ZnO, COD=2300112；Q=quartz, COD=1011172).

Fig. 4 shows the XRD patterns of the samples with 5 wt% internal chloride before and after cold-water extraction for water-soluble chloride. The difference between Fig.3 and Fig.4 raised by the increase in chloride content was the increased peak intensity of NaCl, whereas the variation in the peak intensity of Ht was insignificant, indicating the stability of Ht in AAMs.

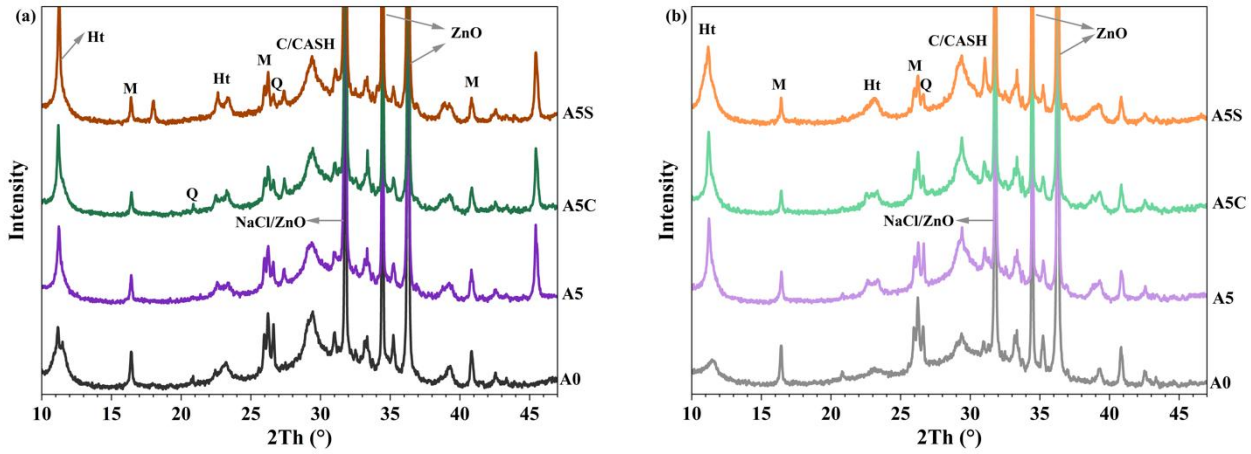


Fig. 4. XRD patterns of samples with 5 wt% internal chloride at 28d (a) before and (b) after cold-water extraction for water-soluble chloride.

To study the influence of water-extraction on the phase assemblage as well as the source phases of extracted chloride, the phase compositions pre- and post-leaching were compared. Fig. 5 shows the quantitative results of the main crystalline phases and the total amorphous phases that include the precursors and gels. It was noted that the R_{wp} values for the Rietveld refinements were within 15%. In Fig.5 (a) before cold-water extraction, the Ht content was 4.2 wt%, 5.6 wt%, 6.3 wt% and 7.1 wt % in A0, A3, A3C and A3S, respectively, while the increase in internal chloride content from 3 wt% to 5 wt% led to insignificant change in Ht content in all samples, indicating limited variation in the chloride binding capacity. Consistent with the increasing NaCl peak intensity, the residual NaCl content increased with raising the NaCl content in the raw materials. According to Fig.5 (b), after the cold-water extraction, the Ht content was decreased from 4.2 wt% to 1.4 wt% in A0, from 6.3 wt% to 5.0 wt% in A3C, and from 7.1 wt% to 5.8 wt% in A3S, whereas the Ht content was increased in A5 and varied slightly in A5C and A5S as compared to the Ht content before cold-water extraction. Moreover, the Ht content was consistently higher in A5 series than that in A3 series after the cold-water extraction. The increase in Ht content could be attributed to the precipitation of Ht during the extraction process.

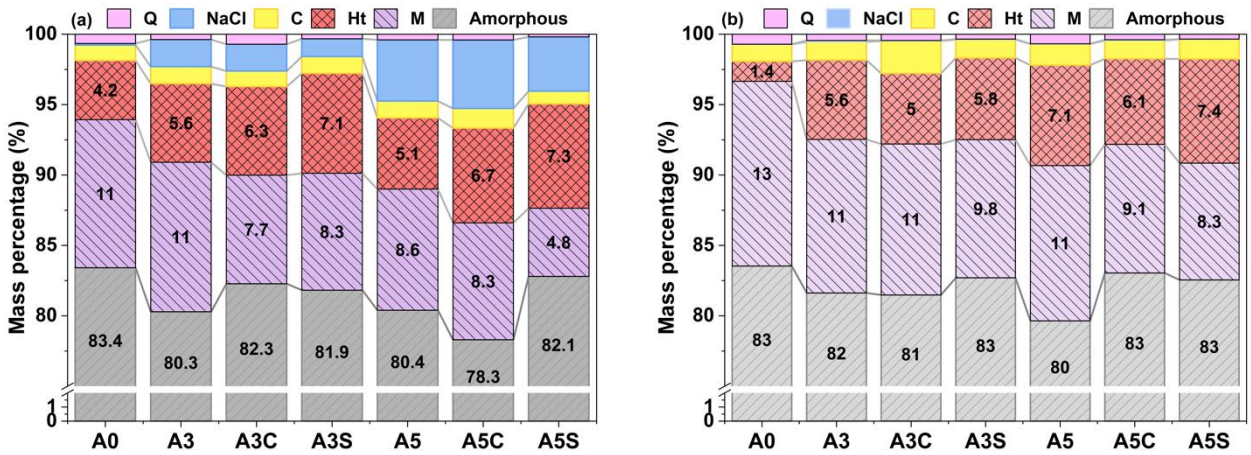


Fig. 5. Mineral compositions of the samples (a) before and (b) after cold-water extraction for water-soluble chloride.

Table 4 shows the leached chloride from extraction (same to the 28-day results in Fig.2) and the chloride in NaCl from QXRD. As seen, for A3 and A3C the two water soluble chlorides match well; for A3S, the chloride sourced from NaCl (quantified by QXRD) was much lower than the extracted chloride, which could be attributed to the release of physically bound chloride by gels and Ht during extraction as indicated by previous study [30]. However, for A5, A5C and A5S, the chloride sourced from NaCl was much higher than the extracted chloride, which probably was attributed to increased chloride binding by hydrates with the dissolution of residual NaCl in the extraction solution, considering that the chloride binding capacity of hydrates could increase with chloride concentration. It was noted that the high content NaCl could remain as solid rather than solute in the limited volume of pore solution.

Table 4. Correlation between leached chloride and chloride in NaCl from QXRD.

	A3	A3C	A3S	A5	A5C	A5S
Leached Cl_w^- (mg/g paste)	11.90	11.60	11.75	18.45	18.60	17.75
Chloride in NaCl (mg/g paste)	11.71	11.59	7.64	26.39	29.48	23.17

3.2.2. TGA

Fig. 6 shows the thermogravimetric (TG) and differential thermogravimetric (DTG) curves of samples with 3 wt% internal chloride before and after cold-water extraction. Gels dehydrated at around 100 ℃, leading to the first peak in DTG curves. Notably, in Fig.6 (a), the first peak became more pronounced with the addition of internal chloride, and the highest peak was found in A3S, followed by A3C and A3. The weak peaks at around 150 ℃ in the DTG curves were attribution to the loss of adsorbed water from Ht, while the peaks at around 350 ℃ in the DTG curves was caused by the dehydroxylation of the octahedral layer and decomposition of interlayer ions that could be hydroxide carbonates, and chloride [36]. The small peaks at around 600 ℃ was related to the decomposition of calcium carbonates, which was formed due to a slight carbonation of the samples during curing or preparation. With the addition of internal chloride in A3, A3C and A3S, new peaks at around 850-950 ℃ were observed, which was attributed to the melting of NaCl. After the cold-water extraction in Fig.6 (b), Ht peaks in the DTG curves were broadened and intensified, which was inconsistent with the decrease in the Ht content in A0, A3C and A3S obtained by QXRD. This change in the DTG peaks of Ht indicated the variation in the crystalline structure, which was difficult to be detected by the XRD pattern of a composite system. Meanwhile, $CaCO_3$ peaks were slightly intensified, suggesting increased carbonation during cold-water extraction. The disappearance of NaCl peaks in Fig.6 (b) confirmed that the cold-water extraction method with a duration of 24h was

sufficient to remove the water-soluble chloride.

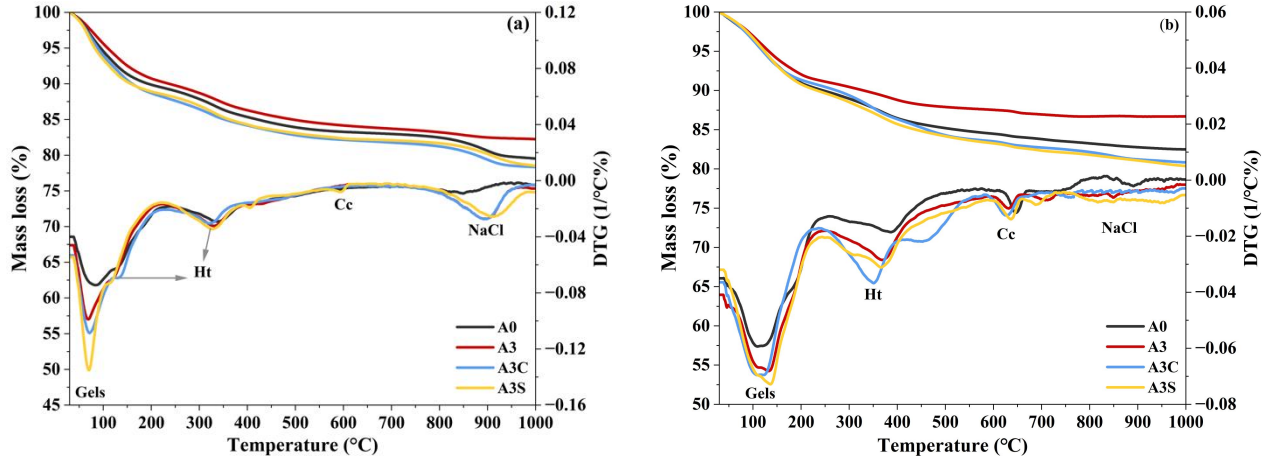


Fig. 6. TG/DTG curves of samples with 3 wt% internal chloride at 28d (a) before and (b) after cold-water extraction for water-soluble chloride.

The TG/DTG curves of samples with 5 wt% internal chloride before and after cold-water extraction were compared in Fig.7. Consistent with Fig.6 (a), the first peak in Fig.7 (a) with the highest intensity was found in the mix with sulfate, i.e., A5S. Besides, the peaks related to NaCl were apparently intensified with increasing the chloride content. From Fig.7 (b), the influence of cold-water extraction on the DTG curves was consistent at two internal chloride contents. Fig. 8 compares the mass loss occurred in a temperature range of 50-550 ℃, which could be used to indicate the difference in hydration degree. The higher mass loss before cold-water extraction in A3 and A5 as compared to that of A0 suggested increased hydration degree by internal chloride, while the comparable mass loss in A3 and A5 indicated that only a lower content than 3 wt% could involve in the hydration, which was consistent with the QXRD results that an increase in chloride content barely altered the Ht content. From the bound water content, the added Na_2CO_3 and gypsum promoted hydration, and a slight greater extent was achieved by gypsum, which was consistent with previous study on the effect of activator on activation of GGBS [37]. Moreover, the mass loss in 50-550℃ from samples after cold-water extraction was consistently lower as compared to that from original samples, which could be attributed to the dissolve of hydrates during extraction.

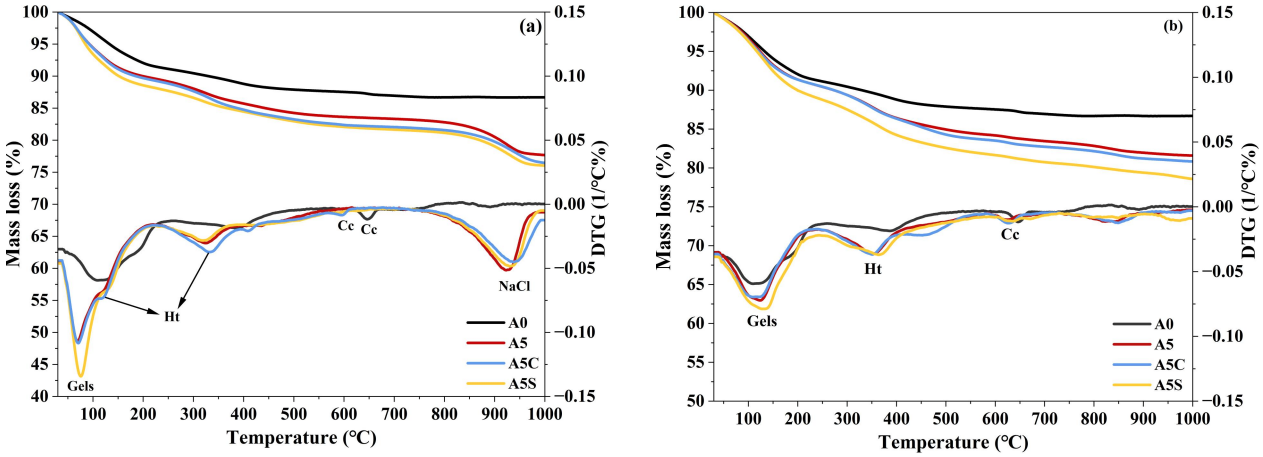


Fig. 7. TG/DTG curves of samples with 5 wt% internal chloride at 28d (a) before and (b) after cold-water extraction for water-soluble chloride.

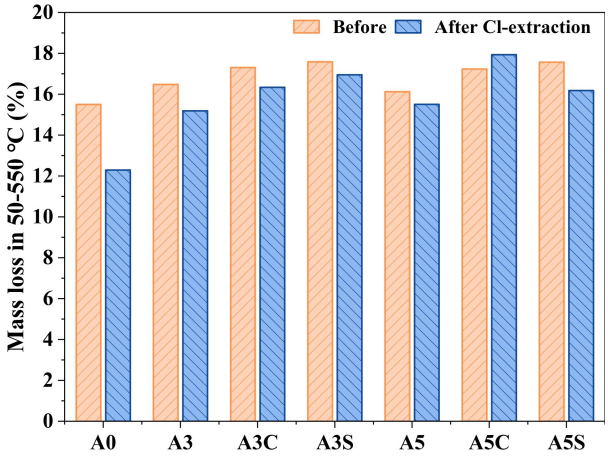


Fig. 8. Mass loss in 50-550℃ from samples (a) before and (b) after water extraction.

3.2.3. The spatial zonation of Cl in Ht

Quantitative SEM-EDS hypermaps analysis was performed to reveal the influence of sulfate and carbonate anions on the spatial zonation of Cl. The BSE image, Ca-Mg-Al composite element map, Cl element map and Cl-S composite element map of A5 and A5S were presented in Fig. 9 and Fig. 10, respectively. In both two Ca-Mg-Al composite element maps, the red, green, and blue channels were assigned to Ca, Mg and Al element, respectively. The GGBS areas were in light red due to the relatively high Ca and Mg concentrations, while FA areas were in dark blue due to a high Al concentration. Besides, bright green rims around GGBS particles were observed, indicating the relatively high Mg concentration. In the Cl element, dispersed bright red rims were found, suggesting a relative high chloride concentration, which confirmed the presence of bound chloride. In the Cl-S composite maps, the green channel was assigned to S element, and the red channel was assigned to Cl element. In A5 activated by NaOH, GGBS was the exclusive source of sulfate, whereby the GGBS areas present with light green in the Cl-S composite map. Besides, bright green rims were

found around GGBS particles due to a relative higher S concentration as compared to GGBS domains. Moreover, it was found most of the bright green rims were in the same location with the high Cl element concentration areas, implying the coexistence of chloride and sulfate in Ht phases that formed around GGBS particles. However, to confirm the involvement of sulfate from GGBS in Ht formation, a further analysis of the chemical compositions in these rims and the dissolution kinetics of GGBS were required, and this was detailed in later sections. In A5S shown in Fig. 10, gypsum provided additional sulfate, which lowered the contrast in sulfate concentration between the matrix and GGBS particles. Thus, the GGBS particles in the Cl-S composite map of A5S presented lighter green than that in A5. Despite the gypsum in A5S, the green rims featured with high S concentration were in similar zonation to those in A5, i.e., clustered around GGBS particles. According to XRD results, gypsum and ettringite were absent in A5S, leading to the inference that intercalation into the Ht phases was probably the only chemical reaction related to sulfate in AAMs and the external sulfate barely altered the preference of S-Ht (Ht with S in the interlayer) precipitation.

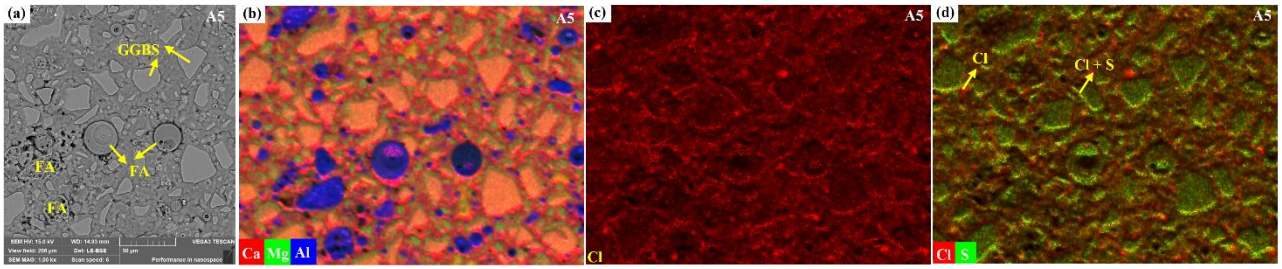


Fig. 9. (a) BSE image, (b) Ca-Mg-Al composite element map, (c) Cl element map, and (d) Cl-S composite element map of A5.

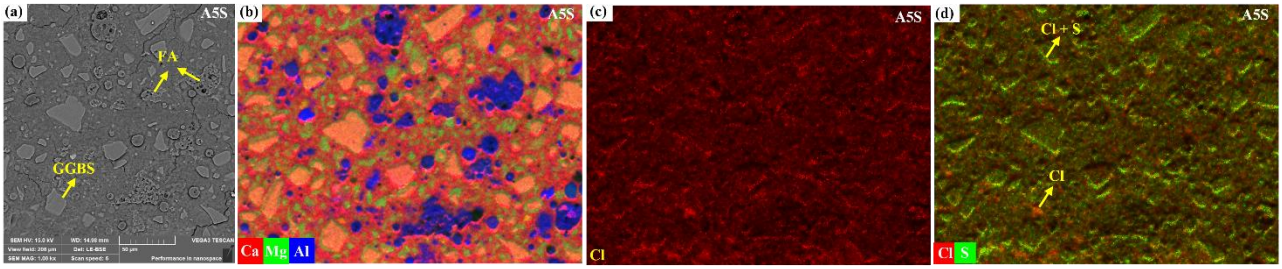


Fig. 10. (a) BSE image, (b) Ca-Mg-Al composite element map, (c) Cl element map, and (d) Cl-S composite element map of A5S.

To achieve phase separation and spatial distribution visualization, the Phate-GMM method proposed in the authors' previous studies [33,34] was applied. In brief, the Phate-GMM algorithm considered the sum of Ca, Al, Mg, Si, Cl, S elements, the relative atom ratios of different two elements and the space distance of each pixel to separate the FA, GGBS, different Ht phases and gels. Fig. 11 (a) and (b) shows the zonation of different phases in A5 and A5S, where the dispersed yellow and green areas denoted with Ca-Al Ht and Mg-Al Ht represent the two types of different Ht. Fig. 11 (c) and (d) shows the Ca/Al vs. Mg/Al atom ratios plot of A5 and A5S, respectively. The Ca-Al Ht areas

were characterized with high Ca/Al atom ratios, while the Mg-Al Ht areas were featured with high Mg/Al atom ratios. The presence of Mg-Al and Ca-Al hydrotalcite-like phases in AAMs was also reported in a previous study [5].

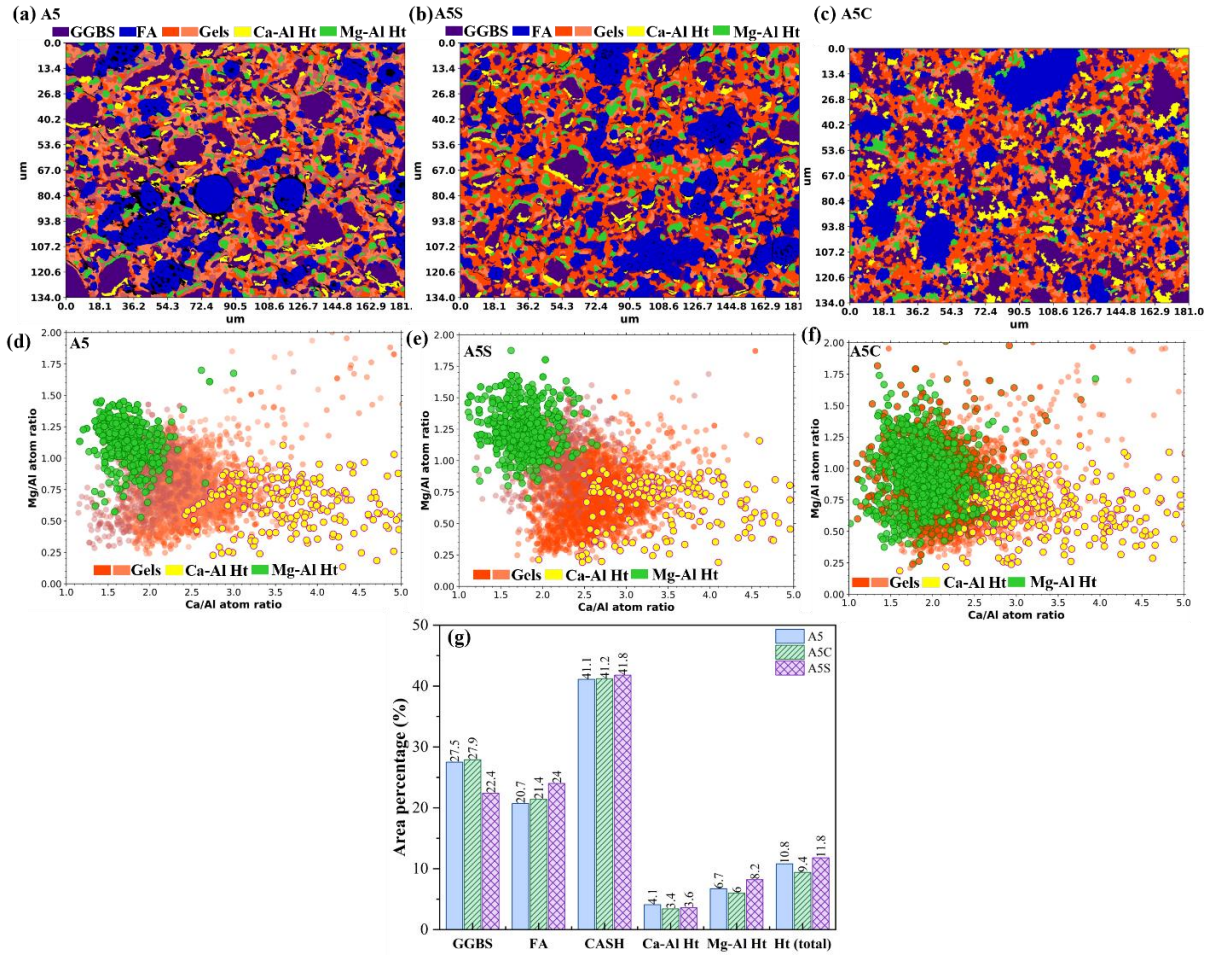


Fig. 11. (a) The identified phase assemblage in (a) A5, (b) A5S, (c) A5C, and Mg/Al vs Ca-Al atom ratios of different phases in (d) A5, (e) A5S, (f) A5C, and (g) the area percentage of different phases.

Fig. 11 (e) compares the area of different phases. It seems that the addition of gypsum in A5S increased the hydration of GGBS, while delayed the reaction of FA. A higher reactivity of GGBS is associated with a faster reaction thus faster consumption of alkalis, reducing the availability of FA to alkalis for activation. However, the difference in the area assigned to gels in A5 and A5S was negligible. The area of Ca-Al Ht and Mg-Al Ht in A5 and A5S was in opposite order, with more Mg-Al Ht identified in A5S. The dissolution of GGBS in AAMs released Mg^{2+} to react with Al^{3+} and anions to form Mg-Al Ht, whereby the higher reaction degree of GGBS resulted more Mg-Al Ht in A5S than that in A5. The total area of Ht was in the same order of the Ht mass content obtained by QXRD, with more Ht being found in A5S, but the value of the area ratio was higher than the mass ratio from QXRD. This could be attributed to the fact that the Ht area was a mixture of multiple products with Ht dominance rather than pure Ht.

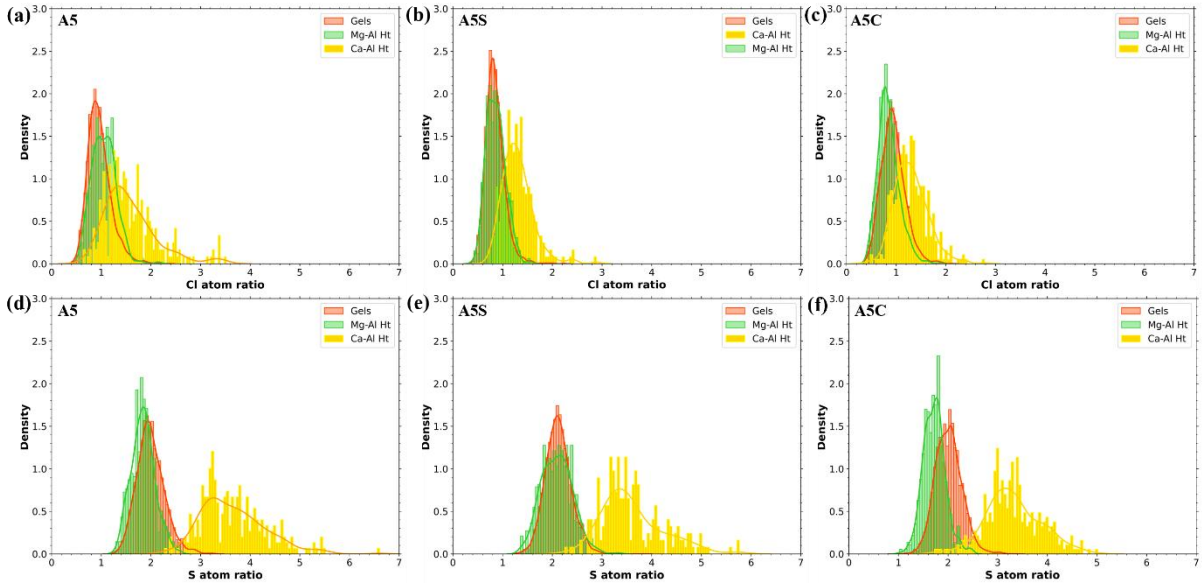


Fig. 12. The histogram of (a) Cl atom ratio in A5, (b) Cl atom ratio in A5S, (c) Cl atom ratio in A5C, (d) S atom ratio in A5, (e) S atom ratio in A5S, and (f) S atom ratio in A5C.

The histogram of Cl atom ratio and S atom ratio in the identified gels and Ht phases were compared in Fig. 12. The mean S and Cl atom ratios (with standard deviations) in Ca-Al Ht and Mg-Al Ht formed in A5, A5S and A5C were tabulated in Table 3. When the mean value was used, the S atom ratio was 2.18-, 2.77- and 2.55-times Cl atom ratio in Ca-Al Ht in A5, A5S and A5C, respectively. Apparently, both the Cl and S atom ratio were higher in Ca-Al Ht as compared to the Mg-Al atom ratio, which suggested that Ca-Al Ht was more favorable for the intercalation of S and Cl. Other than that, despite the sulfate addition, the difference in the distribution of S and Cl atom ratio in three systems was negligible from a statistical point of view. Moreover, the Cl atom ratio was consistently lower than S atom ratio in two systems, indicating that the sulfate from either GGBS or the gypsum was more readily than the chloride to occupy the interlayer of Ht.

Table 3. Mean value and standard deviations of Cl atom ratio and S atom ratio.

Phases	Cl atom ratio		S atom ratio	
	Mean value	Standard deviation	Mean value	Standard deviation
Ca-Al Ht in A5	1.79	0.60	3.90	0.74
Ca-Al Ht in A5S	1.30	0.31	3.60	0.62
Ca-Al Ht in A5C	1.30	0.33	3.31	0.56
Mg-Al Ht in A5	1.05	0.24	1.84	0.24
Mg-Al Ht in A5S	0.88	0.20	2.09	0.31
Mg-Al Ht in A5C	1.02	0.28	2.72	0.39

3.2.4. Discussion

The results reveal that the influence of CO_3^{2-} and SO_4^{2-} on the chloride binding capacity of AAMs was governed by a trade-off between the promotion of hydrotalcite (Ht) formation and the competition for its interlayer sites. Both anions promoted GGBS hydration and increased the Ht content from 5.6 wt% (A3) to 6.3 wt% (A3C, with carbonate) and 7.1 wt% (A3S, with sulfate). Despite this common effect, the two anions acted oppositely: at 5 wt% internal Cl^-, carbonates reduced the bound chloride, whereas sulfate increased it. The reduction in bound chloride caused by carbonate, in spite of the promoted Ht formation, can be rationalized by the higher affinity of CO_3^{2-} for the Ht interlayer. In the anion stability sequence, CO_3^{2-} is the most readily accommodated anion; its preferential intercalation therefore displaces chloride from the interlayer and lowers the chloride binding per unit Ht, outweighing the benefit of the promoted Ht formation. The net consequence is a slightly reduced bound chloride content [8].

By contrast, although sulfate also competes with chloride for intercalation into Ht (the Cl atom ratio was consistently lower than the S atom ratio, and the sulfate released from dissolved GGBS competed with chloride for the interlayer sites), the promotion of Ht formation by sulfate more than compensated for this competition, producing a net increase in bound chloride. The stronger hydration-enhancing effect of gypsum, indicated by a slightly greater bound-water content than that of Na_2CO_3, led to more Mg-Al Ht and a larger overall interlayer reservoir, so that the additional chloride binding exceeded the loss caused by competition. Since gypsum and ettringite were absent in the sulfate-bearing systems, the intercalation into Ht was identified as the only chemical reaction associated with sulfate in these AAMs.

Both effects diminished as curing proceeded: with prolonging the curing time from 7 d to 28 d, the influence of carbonate and sulfate on chloride binding decreased, and at the lower internal chloride content of 3 wt% the influence became negligible (the water-soluble chloride of A3, A3C and A3S fell within 11.60–11.90 mg/g paste). This suggests that the continued hydration enlarged the Ht reservoir over time and that, when the chloride supply was sufficient to saturate the available interlayer sites, the interfering role of the two anions was largely suppressed.

In summary, these findings demonstrate that achieving a high chloride binding by Ht in AAMs containing municipal solid waste incineration fly ash requires not only maximizing Ht formation but also minimizing the competition from interfering anions. In particular, stabilizing the sulfate released from GGBS and gypsum by other phases rather than by Ht is vital to reserve the interlayer sites for chloride and thereby to secure the chloride binding capacity.

4. Conclusions

In this study, alkali-activated slag and fly ash with different levels of internal Cl^-, SO_4^{2-} and CO_3^{2-}

were prepared to reveal their influence on chloride binding, the formation, spatial zonation and chemistry of Ht. The influence of cold water-extraction parameters on free chloride quantification in AAMs was studied. According to the experimental results, the following conclusions were obtained:

(1) The cold-water extracted soluble Cl^- from powder samples increased with prolonging the extraction time from 20 min to 2 h but decreased as the time increased further to 24 h due to continued hydration; from particle samples, the same trend was observed with increasing extraction time from 2 d to 7 d and further to 14 d. The difference in the maximum soluble Cl^- content extracted from powder and particles was less than 5%.

(2) The reduction (44-45%) in cold-water soluble Cl^- extracted from 7-day and 28-day cured samples confirmed the chloride binding capacity of AAMs, which was enhanced by SO_4^{2-} and was reduced by CO_3^{2-}. However, the difference in chloride binding capacity decreased with curing time and was limited to 3.7-10.2%. The chloride binding capacity reached its maximum at 3 wt% internal Cl^- and did not increase further with raising the Cl^- from 3 to 5 wt%.

(3) The presence of Cl^-, SO_4^{2-}, CO_3^{2-} increased Ht formation from 4.2 wt% in A0 to 5.6 wt%, 6.3 wt% and 7.1 wt % in A3, A3C, and A3S, respectively, while increasing the internal Cl^- from 3 wt% to 5 wt% barely affected Ht content and thus the chloride binding. The increased Ht formation was attributed to increased GGBS hydration, which provided more dissolved Mg^{2+}. Cold water-extraction varied the phase assemblage owing to dissolution.

(4) More Mg-Al Ht than Ca-Al Ht was identified around GGBS particles according to the quantitative SEM-EDS hypermaps analysis. Between the two types Ht, Ca-Al Ht showed higher ability to bind Cl^- and SO_4^{2-}, and the statistic distribution of S and Cl in Ht formed in AAMs was probably independent of the relative concentration of two anions in the raw materials. This phenomenon revealed that the SO_4^{2-} from dissolved GGBS competed with Cl^- for intercalation into Ht, reducing the chloride binding capacity.

It was notified that in the Phate-GMM method, only one field of view was analyzed and the comparison given in the current study was only able to reflect one possible trend. In the future work, to provide more statistically meaningful results, many independent fields of view should be analyzed.

Acknowledgements

The authors highly appreciate the financial support from National Natural Science Foundation of China (Grant No. 52408296 and 52308287), the Natural Science Foundation of Hebei Province (E2023203211), and the Education Department of Hebei Province (BJ2025027).

Data availability

All data needed to support the conclusions in the paper are presented in the manuscript. Additional data related to this paper may be available from the corresponding author upon request.

Declaration of competing interest

The authors declare that they have no known competing financial interests or personal relationships that could have appeared to influence the work reported in this paper.

Author contribution statement

Yu Chen: Data curation; Formal analysis; Investigation; Writing – original draft. **Dezhi Zhao:** Data curation; Investigation; Methodology; Writing – review & editing. **Teng Ma:** Data curation; Investigation; Methodology. **Zhengxin Chen:** Writing – original draft; Writing – review & editing. **Caihong Xue:** Data curation; Formal analysis; Funding acquisition; Investigation; Project administration; Writing – original draft; Writing – review & editing. **Qingxin Zhao:** Funding acquisition; Investigation; Writing – original draft; Writing – review & editing.

Use of AI statement

None.

References

[1] Z. Yao, R. Pal, H. Song, A. Van de Keere, A. Kashani, E. Gruyaert, T. Kim, Chloride transport, binding, and microstructure in alkali-activated concrete with different types of precursor combinations, Cem. Concr. Res. 198 (2025) 108002, 10.1016/j.cemconres.2025.108002.

[2] S. Blotevogel, L. Doussang, M. Poirier, L. André, A. Canizarès, P. Simon, V. Montouillout, J. Kaknics, C. Patapy, M. Cyr, The influence of Al2O3, CaO, MgO and TiO2 content on the early-age reactivity of GGBS in blended cements, alkali-activated materials and supersulfated cements, Cem. Concr. Res. 178 (2024) 107439, 10.1016/j.cemconres.2024.107439.

[3] A. Machner, M. Zajac, M. Ben Haha, K.O. Kjellsen, M.R. Geiker, K. De Weerdt, Chloride-binding capacity of hydrotalcite in cement pastes containing dolomite and metakaolin, Cem. Concr. Res. 107 (2018) 163-181, 10.1016/j.cemconres.2018.02.002.

[4] D. Wang, J.L. Provis, B. Lothenbach, S.V. Churakov, B. Ma, Fe(II)-doped hydrotalcite in cement systems: Structure and Cr(VI) immobilization, Cem. Concr. Res. 208 (2026) 108352, 10.1016/j.cemconres.2026.108352.

[5] Z. Yue, X.Q. Wang, X. Zhu, Mineralogical evaluations in 11 KOH-GGBS pastes within 4 years, Cem. Concr. Res. 205 (2026) 108235, 10.1016/j.cemconres.2026.108235.

[6] D. Wang, Y. Zhang, J.L. Provis, B. Lothenbach, S.V. Churakov, G. Miron, Z. Zhou, J. Guan, J. Ban, B. Ma, Hydrotalcite-pyroaurite solid solution in cement system: Molecular structure and thermodynamic properties, Cem. Concr. Res. 197 (2025) 107976,

10.1016/j.cemconres.2025.107976.

[7] L. Yang, M. Chen, Z. Lu, Y. Huang, J. Wang, L. Lu, X. Cheng, Synthesis of CaFeAl layered double hydroxides 2D nanosheets and the adsorption behaviour of chloride in simulated marine concrete, Cement and Concrete Composites. 114 (2020) 103817, 10.1016/j.cemconcomp.2020.103817.

[8] E. Bernard, W.J. Zucha, B. Lothenbach, U. Mäder, Stability of hydrotalcite (Mg-Al layered double hydroxide) in presence of different anions, Cem. Concr. Res. 152 (2022) 106674, 10.1016/j.cemconres.2021.106674.

[9] Y. Jo, P.G. Szabo, R.E. Guidone, B. Lothenbach, N. Çevirim-Papaioannou, E. Coppens, M. Altmaier, X. Gaona, Effect of limestone and sulfate on the uptake of chloride and isosaccharinic acid by high-slag cement paste (CEM III/C), Cem. Concr. Res. 205 (2026) 108212, 10.1016/j.cemconres.2026.108212.

[10] H. Li, X. Hu, M.J. Garba, D. Zhu, C. Shi, Physical adsorption and chemical binding of chloride in the laminate and interlayer of recrystallized hydrotalcite, Cem. Concr. Res. 204 (2026) 108213, 10.1016/j.cemconres.2026.108213.

[11] Z. Xu, Y. Wu, Z. Zhang, Y. Wang, J. Hu, Y. Ma, Z. Zhang, H. Huang, J. Wei, C. Shi, Q. Yu, Insight into ion exchange behavior of LDHs: Asynchronous chloride adsorption and intercalated ions release processes, Cement and Concrete Composites. 147 (2024) 105433, 10.1016/j.cemconcomp.2024.105433.

[12] F. Shen, G. Liu, Y. Zhang, C. Liu, Molecular insights into sulfate-induced chloride release from Friedel's salt, Cem. Concr. Res. 199 (2026) 108042, 10.1016/j.cemconres.2025.108042.

[13] P.W. Brown, S. Badger, The distributions of bound sulfates and chlorides in concrete subjected to mixed NaCl, MgSO4, Na2SO4 attack, Cem. Concr. Res. 30 (10) (2000) 1535-1542, 10.1016/S0008-8846(00)00386-0.

[14] J. Xu, C. Zhang, L. Jiang, L. Tang, G. Gao, Y. Xu, Releases of bound chlorides from chloride-admixed plain and blended cement pastes subjected to sulfate attacks, Constr. Build. Mater. 45 (2013) 53-59, 10.1016/j.conbuildmat.2013.03.068.

[15] M. Guo, Z. Wang, J. Xiao, D. Chen, Z. Lv, The role of hydrotalcite in the chloride binding of hydrated C3A pastes containing dolomite, Constr. Build. Mater. 402 (2023) 132975, 10.1016/j.conbuildmat.2023.132975.

[16] T. Yang, Z. Zhang, F. Zhang, Y. Gao, Q. Wu, Chloride and heavy metal binding capacities of hydrotalcite-like phases formed in greener one-part sodium carbonate-activated slag cements, J. Clean. Prod. 253 (2020) 120047, 10.1016/j.jclepro.2020.120047.

[17] T. Schade, F. Bellmann, B. Middendorf, Quantitative analysis of C-(K)-A-S-H-amount and hydrotalcite phase content in finely ground highly alkali-activated slag/silica fume blended cementitious material, Cem. Concr. Res. 153 (2022) 106706, 10.1016/j.cemconres.2021.106706.

[18] D. Wang, Z. Zhang, W. Guo, J. Li, X. Li, Q. Zhao, A novel all-solid-waste binder prepared by salt-

alkali synergistic activation system constructed from phosphogypsum, soda residue and calcium carbide slag, Cement and Concrete Composites. 155 (2025) 105841, 10.1016/j.cemconcomp.2024.105841.

[19] H. Liu, Y. Zhang, T. Ma, Y. Chen, G. Gu, C. Chen, Valorization of MSWI fly ash via geopolymerization: CLDH-induced multi-pathway immobilization of chloride ions and microstructural evolution, Cement and Concrete Composites. 173 (2026) 106746, 10.1016/j.cemconcomp.2026.106746.

[20] Y. Xing, B. Wang, Y. Xu, H. Yu, Z. Han, J. Zou, Effects of chloride and sulfate contents on the microstructure of AAMs and leaching behavior of heavy metals, Cement and Concrete Composites. 174 (2026) 106791, 10.1016/j.cemconcomp.2026.106791.

[21] Z. Zhang, Z. Zhou, H. Zhu, P. Duan, Y. Fang, Z. Jiang, Mechanisms of CLDH seeding on hydration kinetics of slag-based geopolymer: Towards aluminosilicate cement phase engineering, Composites Part B: Engineering. 271 (2024) 111157, 10.1016/j.compositesb.2023.111157.

[22] Y. Jia, C. Xue, D. Zhao, Q. Zhao, F. Qu, The role of NaCl from municipal solid waste incineration fly ash in alkali-activated materials, Sustain. Mater. Technol. 48 (2026) e02087, 10.1016/j.susmat.2026.e02087.

[23] C. Xue, W. Zhang, Q. Zhao, The role of Al2O3, MgO and CaO in promoting Cl- uptake by hydrotalcite-like phases in alkali-activated binders with MSWI FA, Constr. Build. Mater. 439 (2024) 137259, 10.1016/j.conbuildmat.2024.137259.

[24] S.A. Bernal, R. San Nicolas, R.J. Myers, R. Mejía De Gutiérrez, F. Puertas, J.S.J. van Deventer, J.L. Provis, MgO content of slag controls phase evolution and structural changes induced by accelerated carbonation in alkali-activated binders, Cem. Concr. Res. 57 (2014) 33-43, 10.1016/j.cemconres.2013.12.003.

[25] S.K. Das, Y. Suda, Reactive MgO enhanced carbonation resistance in Alkali-Activated Materials: Insights into Mg-bearing phase evolution and possible M-S-H formation, Cement and Concrete Composites. 170 (2026) 106572, 10.1016/j.cemconcomp.2026.106572.

[26] T. Liu, Q. Yu, H.J.H. Brouwers, In-situ formation of layered double hydroxides (LDHs) in sodium aluminate activated slag: The role of Al-O tetrahedra, Cem. Concr. Res. 153 (2022) 106697, 10.1016/j.cemconres.2021.106697.

[27] T. Liu, S. Li, Y. Chen, H.J.H. Brouwers, Q. Yu, In-situ formation of layered double hydroxides in MgO–NaAlO2-activated GGBS / MSWI BA: Impact of Mg2+ on reaction mechanism and leaching behavior, Cement and Concrete Composites. 140 (2023) 105114, 10.1016/j.cemconcomp.2023.105114.

[28] R. Jia, Y. Chen, S. Jiu, S. Zhuang, Regulating the workability of NaOH-activated blast furnace slag pastes by considering the mutual inhibition between calcium-sodium aluminosilicate hydrate and hydrotalcite during precipitation, Cement and Concrete Composites. 160 (2025) 106022, 10.1016/j.cemconcomp.2025.106022.

[29] H.A. Abdel-Gawwad, T. Hirsch, C. Lehmann, D. Stephan, Layered double hydroxides-based binders: Performance, reaction mechanism, and thermodynamic modelling, Cement and Concrete Composites. 166 (2026) 106400, 10.1016/j.cemconcomp.2025.106400.

[30] X. Xu, X. Hu, M.T. Ghafoor, C. Shi, Effect of extraction parameters and supplementary cementitious materials on rapid determination of free chloride content in cement pastes, Cem. Concr. Res. 208 (2026) 108338, 10.1016/j.cemconres.2026.108338.

[31] P.R. de Matos, J.S. Andrade Neto, C.E.M. Campos, R. Snellings, R.E. Dinnebier, A.P. Kirchheim, Polymorph and minor phase quantification in Portland clinker by X-ray powder diffraction analysis: Addressing challenges and foreign ion effects, Cem. Concr. Res. 190 (2025) 107801, 10.1016/j.cemconres.2025.107801.

[32] F. Georget, W. Wilson, K.L. Scrivener, edxia: Microstructure characterisation from quantified SEM-EDS hypermaps, Cem. Concr. Res. 141 (2021) 106327, 10.1016/j.cemconres.2020.106327.

[33] W. Zhang, Y. Jia, C. Xue, Effect of MgO on the spatial phase assemblage in alkali-activated GGBS from quantified SEM-EDS hypermaps by PHATE-GMM, Constr. Build. Mater. 489 (2025) 142269, 10.1016/j.conbuildmat.2025.142269.

[34] C. Xue, Y. Jia, D. Zhao, W. Zhang, Q. Zhao, Contribution of in-situ Layered Double Hydroxides formation to internal chloride immobilization in alkali-activated GGBS: Effect of Ca/Al and Mg/Al ratio, Constr. Build. Mater. 530 (2026) 146600, 10.1016/j.conbuildmat.2026.146600.

[35] X. Xu, Y. Zhao, X. Hu, M.T. Ghafoor, C. Shi, Effect of water extraction on desorption of bound chloride in Portland cement paste with internally mixed chloride, Cement and Concrete Composites. 169 (2026) 106538, 10.1016/j.cemconcomp.2026.106538.

[36] J. Ban, B. Lothenbach, J.L. Provis, G.D. Miron, Z. Zhou, D. Wang, S.V. Churakov, B. Ma, Examining the pH dependence of Fe behavior in hydrotalcite-group structures, Cem. Concr. Res. 201 (2026) 108097, 10.1016/j.cemconres.2025.108097.

[37] S.A. Bernal, J.L. Provis, R.J. Myers, R. San Nicolas, J.S.J. van Deventer, Role of carbonates in the chemical evolution of sodium carbonate-activated slag binders, Mater. Struct. 48 (3) (2015) 517-529, 10.1617/s11527-014-0412-6.

Author biography



Yu Chen is a PhD candidate at, Yanshan University, China.



Caihong Xue (Corresponding author) is an associate professor and doctoral supervisor at the State Key Laboratory of Metastable Materials Science and Technology, Yanshan University. She obtained her Ph.D. from University of Technology, Sydney. Her research interests include low-carbon alkali-activated materials, harmless synergistic disposal of municipal solid waste incineration fly ash, formation and anion-adsorption performance of in-situ hydrotalcite-like phases. She hosts National Natural Science Foundation projects and has published plenty of relevant academic articles.